Journal of Materials Chemistry C

PAPER

Published on 26 June 2026

Check for updates

Cite this: DOI: 10.1039/d6tc00531d

High-performance broadband photodetection enabled by a GeP/MoS_2 van der Waals p–n heterostructure

Arslan Rehmat,†[a] Muhammad Asim,†[b] Muhammad Farooq Khan, †[c] Muhammad Hamza Pervez, [d] Abdullah A. Al-Kahtani,[e] Muhammad Asghar Khan,[f] Muhammad Abubakr,[g] Muhammad Nasim,[c] Farooq Ahmad,[h] Saddam Aslam,[i] Zeeshan Haider*[j] and Ehsan Elahi *[a]

Received 18th February 2026, Accepted 25th June 2026

DOI: 10.1039/d6tc00531d

rsc.li/materials-c

van der Waals (vdW) heterostructures based on two-dimensional (2D) semiconducting materials have been thoroughly investigated for practical applications. Recent studies on 2D materials have reignited interest in p–n junctions, with promising potential for applications in both electronics and optoelectronics. Here, we present a photodiode using a p-type GeP/n-type MoS_2 heterostructure with a strong diode rectification of 2.1×10^4, which confirms the creation of a high-quality p–n junction. The device has a high responsivity of about 754 A W^{-1} and a high external quantum efficiency (EQE) of about 5.35×10^4 at a bias of 1 V along the source–drain. Photocurrent mapping shows intrinsic photovoltaic behaviour with a photocurrent of 0.39 μA under zero bias conditions, which is enhanced to 0.60 μA under reverse bias conditions and suppressed under forward bias conditions, which provides evidence of junction-dominated carrier separation. The measured photoresponse is sub-linear within a power-law with an exponent α = 0.65, and a stable response of the device with a rise and decay time of 165 milliseconds and 206 milliseconds, respectively, is achieved. These results point to the GeP/MoS_2 vdW heterostructure as a potential platform for high-performance visible light photodetectors with the possibility of extending into the near-infrared region.

1. Introduction

Two-dimensional (2D) layered materials have emerged as a powerful platform for next-generation electronic and optoelectronic devices owing to their atomic-scale thickness, van der Waals (vdW) bonding, and dangling-bond-free surfaces.[1–5] vdW heterostructures offer the additional advantage of remarkable flexibility in engineering the band alignment and interfacial electrostatic fields, which are critically important for the efficient separation and transport of charge carriers.[6–8] Therefore, heterostructures involving 2D materials have been extensively studied as photodetectors, photovoltaics, and other optoelectronic devices in which the interface-oriented processes play critical roles in device functionality.[9–13] Among various 2D semiconductors, molybdenum disulfide (MoS_2) has been extensively studied because of its layer-dependent bandgap, which evolves from an indirect gap (~1.2 eV) in the bulk to a direct gap (~1.9 eV) in the monolayer, making it highly suitable for visible-light detection.[14] Moreover, MoS_2 exhibits strong light–matter interactions, and the electronic properties of the material are favorable for device integration. However, photodetectors made of MoS_2 are often inherently limited, including low optical

[a] Department of Inorganic Chemistry, University of Chemistry and Technology Prague, Prague 616628, Czech Republic. E-mail: elahie@vscht.cz
[b] Department of Physics & Astronomy, Sejong University, Seoul 05006, Republic of Korea
[c] Department of Semiconductor Systems Engineering, Sejong University, Seoul 05006, Republic of Korea
[d] Institute of Information and Communication Technologies, Electronics and Applied Mathematics, Université catholique de Louvain, 1348 Ottignies-Louvain-la-Neuve, Belgium
[e] Chemistry Department, College of Science, King Saud University, P.O. Box 2455, Riyadh, 11451, Saudi Arabia
[f] Division of Electronics and Electrical Engineering, Dongguk University, Seoul 04620, Republic of Korea
[g] Department of Materials Engineering and Convergence Technology, Gyeongsang National University, Jinju, Gyeongsangnam-do 52828, Republic of Korea
[h] Centre of Excellence in Solid State Physics, University of the Punjab, Lahore, Pakistan
[i] Department of Physics, Riphah International University, Campus Lahore, Pakistan
[j] Department of Physics and Semiconductor Science, Gachon University, Seongnam-si 13120, Republic of Korea. E-mail: zeeshanhaider@gachon.ac.kr
† These authors contributed equally.

absorption due to their atomic-scale thickness, relatively high dark current, and low detectivity with external bias.[15–17] These constraints significantly limit the ability of the devices under the low-light conditions, which in turn has led to the creation of heterostructure-based photodiodes that aim at improving the separation of the carriers and reducing the recombination losses.[18–21] Photodiode-based photodetectors based on p–n junctions can be a feasible approach to overcome these hindrances, as they take advantage of the inherent electric field at the junction interface to dissociate photogenerated carriers.[22–25] In vdW p–n heterostructures assembled by stacking intrinsically p-type and n-type 2D semiconductor sheets, the built-in potential at the junction drives directional charge-carrier transport, suppresses interfacial recombination, and yields a stable, well-defined photoresponse without the need for complex electrostatic gating or chemical doping.[26,27] Such devices are often driven with a relatively low external bias in order to raise the collection of carriers, but the fact that a significant photocurrent is observed at zero bias is important evidence of good junction quality and efficient separation of charges using internal electric fields.[28,29] Germanium phosphide (GeP) is a new layered semiconductor with intrinsic p-type conductivity with a narrow bandgap of about 0.83 eV, thus being especially interesting for extending photodetection to the near-infrared (NIR) spectral range.[30]

In this work, we demonstrate a GeP/MoS_2 vdW p–n heterostructure photodetector exhibiting clear diode-like behavior with a rectification ratio (RR) of 2.1×10^4, confirming the formation of a high-quality junction. Upon application of drain–source bias of 1 V, the device delivers a high responsivity (R) of 754 A W^{-1}, a large external quantum efficiency (EQE) of 5.35×10^4% under 455 nm illumination. Furthermore, photocurrent mapping reveals a finite photocurrent of approximately 0.39 μA at zero bias, evidencing efficient built-in-field-assisted carrier separation at the heterointerface. These results highlight the effectiveness of the GeP/MoS_2 vdW p–n heterostructure for high-sensitivity visible-light photodetection while offering a promising route toward broadband photodetectors with potential IR detection capability.

2. Device fabrication

A conventional dry-transfer method was used to fabricate the GeP/MoS_2 vdW heterojunction device. Thin GeP flakes were first mechanically exfoliated from bulk crystals (from HQ graphene) onto a PDMS stamp using adhesive tape and transferred onto a Si/SiO_2 substrate. Subsequently, few-layer MoS_2 flakes were exfoliated onto a PDMS stamp and carefully aligned and transferred onto the GeP flake under an optical microscope using a micromanipulator-assisted transfer system. The source and drain electrodes were patterned using electron-beam lithography, followed by thermal evaporation of Cr/Au (5/50 nm) to form electrical contacts. The morphology and the overlap region of the GeP/MoS_2 heterostructure were examined using optical microscopy, scanning electron microscopy (SEM), and Raman. Electrical and optoelectronic measurements were performed at room temperature using a Keithley measurement system under high-vacuum conditions. Scanning photocurrent mapping was carried out under 405 nm laser excitation with an incident optical power of 6.73 μW, and the laser spot size was estimated to be approximately 1 μm in diameter from the spatial resolution of the photocurrent map.

3. Results and discussion

3.1. Structural and spectroscopic characterization

The structural configuration and material characterization of the GeP/MoS_2 is presented in Fig. 1. A schematic illustration of the device architecture is shown in Fig. 1a, where the GeP flake is positioned at the bottom, and the MoS_2 flake is stacked on top, forming a vertical p–n junction on a Si/SiO_2 substrate. The overlapping region between GeP and MoS_2 defines the active junction area, while the metal electrodes provide independent electrical contacts to each layer. An optical microscope image and a scanning electron microscope image of a representative GeP/MoS_2 heterostructure device are displayed in Fig. 1b and c. The image clearly reveals a well-defined overlap region with sharp flake boundaries, indicating successful assembly of the heterostructure through a dry-transfer process. Although localized bubbles (trapped air pockets) are observed at the overlapped region, a well-documented artifact of the deterministic dry-transfer assembly that remains confined to localized, non-active areas of the active overlap region is free of visible cracks or contamination, indicating good interlayer contact essential for efficient charge transport across the junction. Raman spectroscopy was employed to further confirm the material quality and phase integrity of the individual components and the assembled heterostructure. Fig. 1d shows the Raman spectrum of the GeP flake, exhibiting its characteristic vibrational modes, consistent with previously reported layered GeP crystals.[31] Fig. 1e presents the Raman spectrum of the MoS_2 flake, where the prominent in-plane E^1_{2g} and out-of-plane A_{1g} modes are clearly observed, confirming the crystalline nature of MoS_2.[32] The Raman spectrum collected from the GeP/MoS_2 overlap region is shown in Fig. 1f. Distinct Raman features from both GeP and MoS_2 are simultaneously present without the emergence of additional peaks or significant peak shifts, indicating that the heterostructure formation preserves the structural integrity of each layer. This observation confirms that the GeP/MoS_2 interface is formed through van der Waals interactions rather than chemical bonding, resulting in a clean and well-defined heterointerface suitable for p–n junction device operation. The thickness of each flake is examined *via* atomic force microscopy (AFM) as shown in Fig. S1(a–d).

3.2. Electrical properties

The transfer characteristic of the MoS_2 device measured at a fixed drain–source voltage of 1 V is shown in Fig. 2a. The drain current increases monotonically with a positive gate voltage, reaching a maximum current of approximately 32.1 μA at

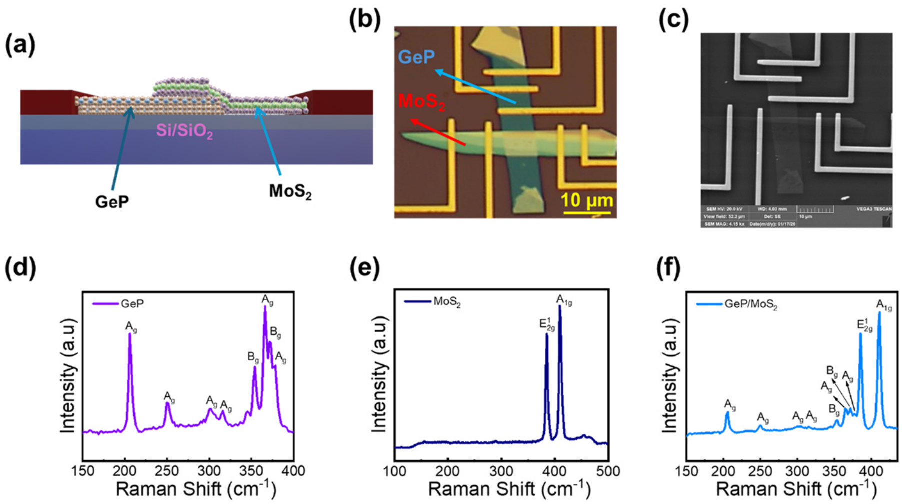

Fig. 1 (a) Schematic illustration of the GeP/MoS_2 vdW p–n heterostructure fabricated on a Si/SiO_2 substrate, showing the device geometry and electrode configuration. (b and c) Optical microscope and SEM image of a representative GeP/MoS_2 heterostructure, where the GeP flake is located at the bottom, and the MoS_2 flake is stacked on top, forming the vertical p–n junction in the overlapping region. (d) Raman spectrum of the GeP flake, confirming its characteristic vibrational modes. (e) Raman spectrum of the MoS_2 flake, exhibiting the typical in-plane and out-of-plane vibrational peaks. (f) Raman spectrum of the GeP/MoS_2 heterostructure, demonstrating the coexistence of Raman features from both constituent materials, indicating successful formation of the vdW heterostructure.

V_g = +60 V, confirming the intrinsic n-type conduction of MoS_2. This behavior arises from gate-induced electron accumulation in the MoS_2 channel under positive gate bias. The corresponding output characteristics presented in Fig. 2b, measured at gate voltages ranging from 0 to +60 V, exhibit clear gate-dependent current enhancement, indicating effective electrostatic modulation of electron transport in MoS_2. In contrast, the GeP device exhibits pronounced p-type behavior, as shown in Fig. 2c. The transfer curve measured at V_{ds} = 1 V shows increasing drain current with negative gate voltage, reaching its maximum at V_g = −60 V, which reflects strong hole accumulation in the GeP channel under negative gate bias. The output characteristics displayed in Fig. 2d, measured at gate voltages between 0 and −60 V, further confirm hole-dominated transport with enhanced current at increasingly negative gate voltages. These results verify the complementary carrier polarities of MoS_2 and GeP, which are essential for forming a high-quality p–n junction. The semi-log plot of the output characteristics of the GeP/MoS_2 heterostructure is shown in Fig. 2e, where clear diode-like rectification is observed, indicating asymmetric carrier transport across the p–n junction. The rectifying behavior originates from band bending[33] and the formation of a depletion region at the GeP/MoS_2 interface after Fermi-level equilibration. Under forward bias, the potential barrier is reduced, allowing efficient carrier injection, whereas under reverse bias, the barrier suppresses current flow.[34,35] The inset, shown on a linear scale, provides a clearer view of the forward-bias regime, illustrating the gradual increase in current with increasing drain voltage and the strong gate-dependent modulation of carrier transport. Fig. 2f presents the gate-voltage-dependent rectification ratio, where a maximum rectification ratio of approximately 2.1×10^4 is achieved at V_g = −60 V, followed by a gradual reduction as the gate voltage increases toward positive values. This behavior can be explained by the gate-controlled modulation of carrier concentrations and the depletion region at the heterointerface. At negative gate voltages, hole accumulation in GeP is significantly enhanced while electron density in MoS_2 is reduced, leading to an expanded depletion region and a higher effective junction barrier under reverse bias. This strongly suppresses reverse current while maintaining forward current, resulting in a high rectification ratio. As the gate voltage becomes more positive, electron accumulation in MoS_2 increases and the depletion region narrows, which reduces the junction barrier and increases reverse-bias leakage current. Consequently, the rectification ratio decreases with increasing gate voltage.[36,37] This gate-tunable rectification behavior confirms that the GeP/MoS_2 heterostructure operates as an electrostatically controllable p–n diode with a high-quality van der Waals interface.

3.3. Broadband photoresponse dynamics

The photodetection performance of the GeP/MoS_2 vdW p–n heterostructure under broadband optical illumination is illustrated in Fig. 3. Fig. 3(a) shows the output characteristics of the GeP/MoS_2 vdW p–n heterostructure under illumination at wavelengths between 365 and 850 nm. The device exhibits clear wavelength-dependent photoresponse, with higher photocurrent at shorter wavelengths and a gradual decrease toward longer wavelengths, reflecting more efficient photogeneration at higher photon energies. The nonlinear and asymmetric behavior of the curves confirms the rectifying nature of the p–n junction, where enhanced current under forward bias arises from efficient carrier injection across the heterointerface. The time-resolved photocurrent response of the GeP/MoS_2 device measured at a drain–source voltage of 1 V is presented in Fig. 3b. The device exhibits stable and repeatable photocurrent

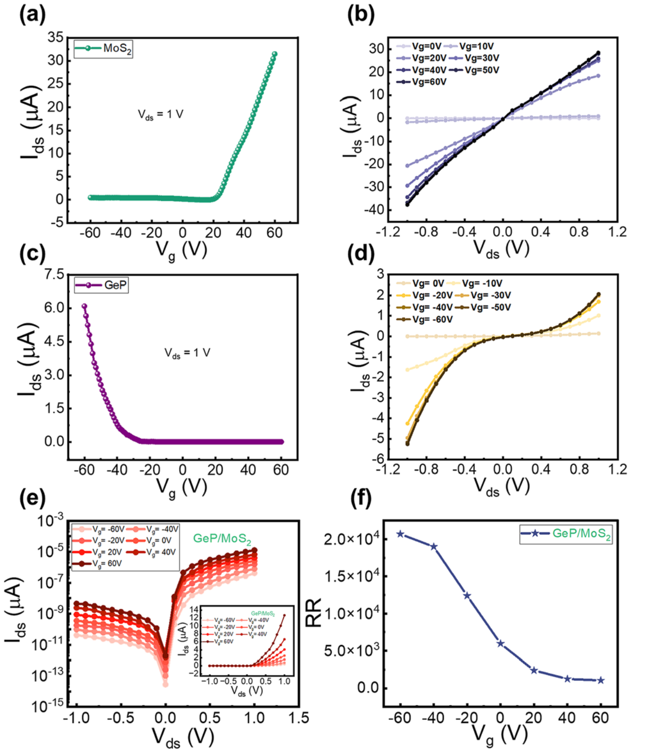

Fig. 2 Electrical characteristics of the individual materials and the GeP/MoS_2 vdW p–n heterostructure device. (a) Transfer characteristic (I_{ds}–V_g) of the MoS_2 channel, showing typical n-type behavior. (b) Output characteristics (I_{ds}–V_{ds}) of the MoS_2 device measured at different gate voltages, confirming gate-tunable electron transport. (c) The transfer characteristic of the GeP channel exhibits pronounced p-type conduction. (d) Output characteristics of the GeP device under various negative gate voltages, demonstrating hole-dominated transport. (e) Semi-log of output characteristics of the GeP/MoS_2 heterostructure under varying gate voltages, revealing pronounced rectifying (diode-like) behavior with asymmetric current response between forward and reverse bias, along with strong gate control over carrier injection across the p–n junction. Inset: linear-scale plot of the same output characteristics, highlighting the forward-bias conduction behavior and gate-dependent current modulation. (f) Gate-voltage-dependent rectification behavior of the GeP/MoS_2 heterostructure, highlighting the tunability of the junction characteristics.

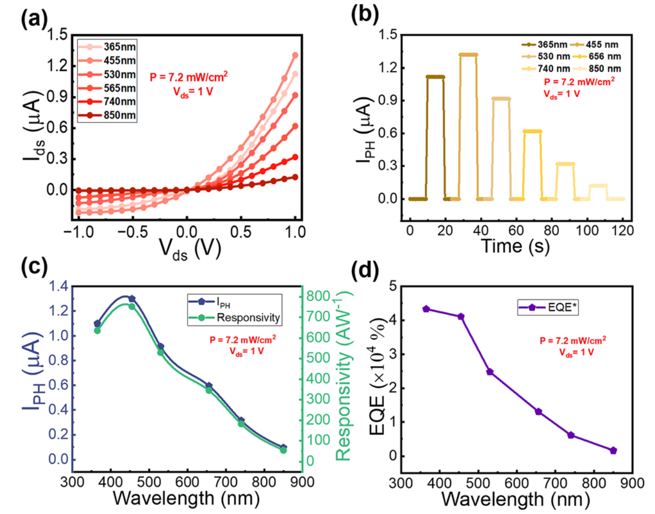

Fig. 3 Photodetection performance of the GeP/MoS_2 vdW p–n heterostructure device. (a) Output characteristics of the GeP/MoS_2 vdW p–n heterostructure photodetector measured under illumination at different wavelengths (365–850 nm) with a fixed optical power density of 7.2 mW cm^{-2} and a drain–source bias condition of 1 V. (b) Time-resolved photocurrent response of the GeP/MoS_2 device measured at a drain–source bias of 1 V under illumination with different wavelengths ranging from 365 to 850 nm at a fixed power density of 7.2 mW cm^{-2}, demonstrating stable and repeatable photoresponse. (c) Wavelength-dependent photocurrent (I_{PH}) and corresponding responsivity (R), showing a strong visible-light response with a peak around 455 nm. (d) Spectral dependence and external quantum efficiency (EQE), revealing enhanced detection performance in the visible region and a gradual decrease toward longer wavelengths.

switching under periodic illumination at different wavelengths ranging from the ultraviolet to the near-infrared region. The reproducible on/off behavior and negligible signal degradation over multiple cycles confirm reliable photodetection and good operational stability. The magnitude of the photocurrent varies with wavelength, reflecting differences in optical absorption, carrier generation, and recombination dynamics across the spectrum.[38]

EQE and D^* were calculated using the following relations:

$$\mathrm{EQE}\ (\%) = \frac{Rhc}{q\lambda} \times 100 \tag{1}$$

where R is the responsivity, h is Planck's constant, c is the speed of light, q is the elementary charge, and λ is the wavelength.

The area of the GeP/MoS_2 overlap junction is determined from the calibrated optical micrograph (Fig. 1b) and the SEM image (Fig. 1c) as $A \approx 4.8\ \mu m \times 6.2\ \mu m \approx 29.8\ \mu m^2$ ($\approx 3.0 \times 10^{-7}\ cm^2$), and this value is used consistently in all R, EQE calculations. Fig. 3c shows the wavelength-dependent photocurrent and the corresponding responsivity extracted at a fixed illumination power density of 7.2 mW cm^{-2}. The device exhibits its maximum photoresponse at 455 nm, where a high responsivity of 754 A W^{-1} is achieved. This enhanced response originates from the strong light absorption of MoS_2 in the visible region, where the photon energy closely matches its direct bandgap, resulting in efficient photocarrier generation. In contrast, the reduced response observed at 365 nm can be attributed to increased surface recombination and higher-energy photon losses near the interface, where photogenerated carriers are more susceptible to trapping and nonradiative recombination before being collected. Additionally, ultraviolet illumination can induce stronger scattering and absorption near the surface, limiting the effective carrier extraction across the heterojunction. The spectral dependence and external quantum efficiency (EQE) is presented in Fig. 3d. At 455 nm, the device reaches a high and a large EQE of 5.35×10^4%, indicating efficient photon-to-carrier conversion and low noise performance. Toward shorter wavelengths, the decrease in EQE is consistent with enhanced recombination and reduced carrier collection efficiency, while the gradual decline at longer wavelengths reflects reduced optical absorption. Notably, the presence of GeP with a narrow bandgap supports photoresponse extending toward the near-infrared region. These results confirm that the GeP/MoS_2 heterostructure operates as an efficient broadband photodetector with optimal sensitivity in the visible spectral range.

3.4. Intensity-dependent photodetection

The intensity-dependent photodetection behavior of the GeP/MoS_2 vdW p–n heterostructure under 455 nm illumination is illustrated in Fig. 4, measured at a fixed drain–source bias of 1 V. Fig. 4(a) shows the output characteristics of the GeP/MoS_2 vdW p–n heterostructure under 455 nm illumination at varying optical power densities (0.76–7.2 mW cm^{-2}). The drain current increases systematically with increasing illumination intensity, indicating enhanced photogeneration of charge carriers at higher incident power. The nonlinear and asymmetric nature of the curves confirms the rectifying behavior of the p–n junction. Under forward bias, the current rises sharply due to efficient carrier injection across the heterointerface, while under reverse bias, the current remains comparatively low due to the presence of a depletion region. These results demonstrate strong light-intensity-dependent photoresponse and efficient carrier separation in the device. The time-resolved photocurrent response measured at incident power densities ranging from 0.76 to 7.2 mW cm^{-2} is presented in Fig. 4b. The device exhibits stable photo-switching behavior at all illumination levels, with the photocurrent increasing systematically as the incident power density increases. At the highest illumination intensity of 7.2 mW cm^{-2}, the photocurrent reaches a maximum value of approximately 1.35 μA, indicating efficient photocarrier generation and collection across the heterojunction. The absence of noticeable baseline drift or signal degradation during repeated on/off cycles confirms good operational stability. Fig. 4c shows the dependence of photocurrent and responsivity on incident optical power, while the photocurrent increases monotonically with increasing power density, the responsivity exhibits a gradual decrease at higher illumination levels. The maximum responsivity of approximately 754 A W^{-1} is achieved at lower optical powers and decreases as the incident intensity increases. This behavior is attributed to the progressive filling of trap states at the GeP/MoS_2 interface and within the layered materials, which reduces photo-gain at higher carrier densities. As the illumination intensity increases further, enhanced carrier–carrier recombination and limited carrier lifetime lead to responsivity saturation. The variation of the external quantum efficiency (EQE) as a function of incident power density is shown in Fig. 4d. The device exhibits a high EQE of 5.35 × 10^4% under low illumination conditions, which gradually decreases with increasing power density. This trend is consistent with increased noise and recombination processes at higher photocarrier concentrations. In addition to intensity-dependent behavior, the temporal response of the GeP/MoS_2 photodetector was evaluated, as shown in Fig. S2. By fitting the rising and falling edges of the photocurrent transients with exponential functions, rise and decay time constants of 165 ms and 206 ms, respectively, were extracted. These response times indicate reliable and repeatable photo-switching behavior, governed by carrier transport across the heterointerface and trapping–detrapping processes within the device. The intensity-dependent photocurrent follows a power-law relationship $I_{ph} \propto P^{\alpha}$, with an extracted exponent of α = 0.65, as summarized in Fig. S3, confirming a sub-linear photoresponse governed by trap-assisted carrier dynamics.

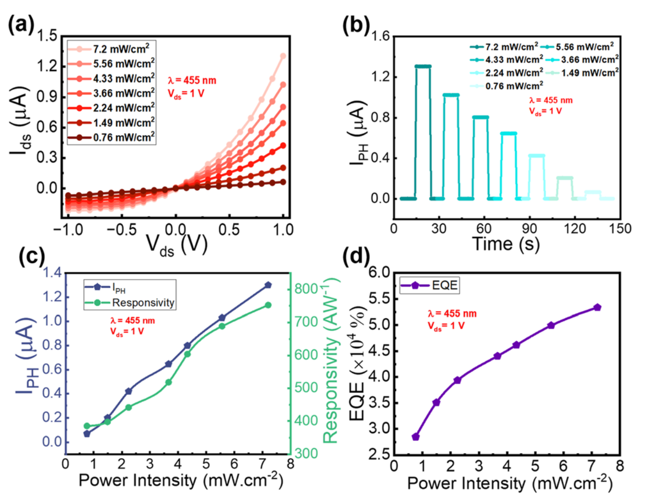

Fig. 4 (a) Output characteristics of the GeP/MoS_2 vdW p–n heterostructure photodetector measured under 455 nm illumination at varying optical power densities (0.76–7.2 mW cm^{-2}) with a fixed drain–source bias condition. (b) Time-resolved photocurrent response measured at a drain–source bias of 1 V under 455 nm illumination with varying incident power densities from 0.76 to 7.2 mW cm^{-2}, demonstrating stable and reproducible photoresponse with increasing light intensity. (c) Dependence of photocurrent (I_{PH}) and responsivity on incident optical power, showing a monotonic increase in photocurrent accompanied by a gradual reduction in responsivity at higher illumination intensities. (d) Variation of external quantum efficiency (EQE) as a function of incident power density, indicating enhanced detection performance at lower illumination levels and saturation behavior at higher powers.

3.5. Photocurrent generation mechanism

The photocurrent generation mechanism of the GeP/MoS_2 vdW p–n heterostructure through schematic band diagrams and spatial photocurrent mapping under different bias conditions is illustrated in Fig. 5. At zero bias (Fig. 5a), Fermi-level equilibration between p-type GeP and n-type MoS_2 leads to band bending at the heterointerface and the formation of a built-in electric field across the depletion region. This internal electric field enables photovoltaic separation of photogenerated electron–hole pairs without external bias.[39,40] The corresponding zero-bias photocurrent map shown in Fig. 5b reveals a localized photocurrent hotspot at the GeP/MoS_2 overlap region, with a measured photocurrent of approximately 0.39 μA. This finite photocurrent confirms efficient built-in-field-assisted carrier separation at the junction and indicates a high-quality vdW interface with suppressed recombination. Under forward bias (+1 V), as illustrated in Fig. 5c, the applied voltage partially compensates for the built-in potential, resulting in reduced band bending and a narrow depletion region. Consequently, the effective electric field responsible for separating photogenerated carriers is weakened. This behavior is reflected in the forward-bias

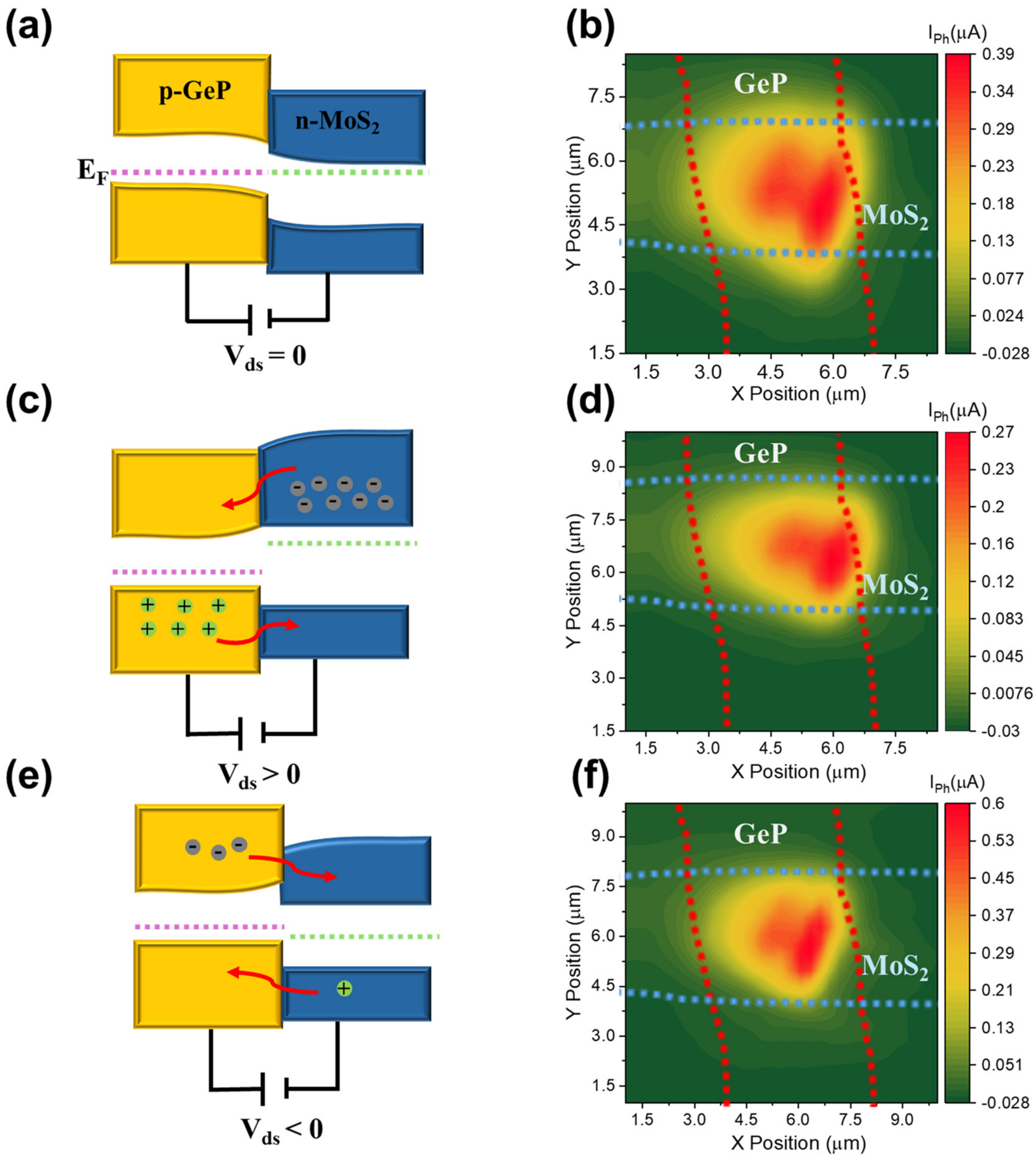

Fig. 5 (a) Schematic band diagram of the p-GeP/n-MoS_2 interface at zero bias, illustrating the built-in electric field established after Fermi-level equilibration. (b) Zero-bias photocurrent map showing a junction-localized photocurrent hotspot generated by the internal electric field, indicating intrinsic carrier separation at the heterointerface. (c) Forward-bias band diagram, where the applied voltage partially compensates for the built-in potential, reduces band bending, and narrows the depletion region, leading to a weakened interfacial electric field. (d) Forward-bias photocurrent map exhibiting a reduced and spatially broadened photoresponse, consistent with suppressed photovoltaic separation and increased majority-carrier transport. (e) Reverse-bias band diagram, where the external bias enhances band bending, enlarges the depletion region, and strengthens the electric field across the p–n junction. (f) Reverse-bias photocurrent map displaying an intensified and spatially confined hotspot at the GeP/MoS_2 overlap region, confirming efficient photocarrier separation and collection under the reinforced electric field.

photocurrent map (Fig. 5d), where the photocurrent decreases to approximately 0.27 μA and becomes more spatially broadened. The reduced photocurrent under forward bias indicates suppressed photovoltaic separation due to the diminished junction electric field and increased recombination. In contrast, when a reverse bias (−1 V) is applied, the band diagram shown in Fig. 5e demonstrates enhanced band bending and an expanded depletion region at the GeP/MoS_2 interface. The strengthened electric field promotes more efficient separation and collection of photogenerated carriers. As a result, the reverse-bias photocurrent map displayed in Fig. 5f shows a strongly intensified and spatially confined photocurrent hotspot at the heterojunction, with a maximum photocurrent of approximately 0.60 μA. This enhancement confirms that reinforcing the built-in electric field under reverse bias significantly improves carrier extraction efficiency.[41] Overall, the bias-dependent photocurrent mapping clearly demonstrates that the photoresponse of the GeP/MoS_2 heterostructure is governed by the strength of the interfacial electric field. While the device exhibits intrinsic photovoltaic behavior at zero bias, the application of reverse bias enhances band bending and depletion width, leading to the highest photocurrent, whereas forward bias weakens the junction field and suppresses the photoresponse. These observations provide direct experimental evidence that the GeP/MoS_2 vdW p–n junction dominates the photodetection mechanism and that carrier separation can be effectively tuned through external biasing.

The present study introduces an intrinsic vdW p–n heterostructure photodetector by combining p-type GeP with n-type MoS_2, avoiding external doping, complex contact engineering, or electrostatic carrier modulation that are commonly employed in 2D photodetectors. The demonstrated junction-dominated photoresponse, gate-tunable rectification, and bias-controlled carrier separation provide direct insight into the interfacial physics governing photodetection in layered heterostructures. Importantly, the incorporation of narrow-bandgap GeP not only enhances charge separation at the junction but also offers a clear pathway for extending photodetection beyond the visible spectrum toward the near-infrared region. Building on these results, future efforts will be focused on optimizing layer thickness, interface quality, and contact configuration to further improve response speed and spectral sensitivity, as well as exploring scalable fabrication routes and integration with flexible or multifunctional device architectures. These directions position GeP-based vdW heterostructures as a promising material platform for next-generation broadband optoelectronic systems.

4. Conclusions

In summary, a vdW p–n heterostructure photodetector with p-type GeP and n-type MoS_2 has been presented. The heterostructure produces a clean and well-defined p–n junction, which shows evident diode-like characteristics and efficient electrostatic tunability, which verifies the quality of vdW interface. The GeP/MoS_2 shows a stable and efficient photoresponse of the visible spectral range with photocurrent generation dominated by the inherent electric field at the heterointerface. Spatial photocurrent mapping and anisotropy in bias dependence quantities indicate that junction electrostatics define carrier separation and collection and give a direct understanding of the mechanism underlying photodetection. Moreover, GeP has a narrow bandgap, which provides a viable path to the development of photodetection in the near-infrared spectrum. In general, this paper has shown that intrinsic two-dimensional vdW p–n heterostructures offer a scalable and efficient platform for high-sensitivity optoelectronic devices.

Author contributions

A. R., M. A., and M. F. K., writing – review and editing, writing – original draft, visualization, validation, methodology, investigation, formal analysis, data curation, conceptualization. M. H. P. and A. A. K.: writing – review and editing, investigation, formal analysis, data curation. M. A. K.: writing – review and editing, methodology, investigation, formal analysis, data curation. M. A.: visualization, validation, investigation, formal analysis, data curation. M. N., F. A. and S. A.: visualization, validation, investigation, formal analysis. E. E. and Z. H.: writing – review and editing, visualization, validation, supervision, software, resources, project administration, investigation, funding acquisition, formal analysis, conceptualization.

Conflicts of interest

The authors state that they have no competing financial or non-financial interests.

Data availability

The data are available upon reasonable request from the corresponding author.

Supplementary information (SI) is available. See DOI: https://doi.org/10.1039/d6tc00531d.

Acknowledgements

The authors thank the Ongoing Research Funding program (ORF-2026-266), King Saud University, Riyadh, Saudi Arabia, for financial support. Author Ehsan Elahi recognizes the funding provided by OP-JAK *via* project number CZ.02.01.01/00/22_010/0013777, ‘‘Chemical Fellows VIII’’. The authors also acknowledge assistance from the Advanced Multiscale Materials for Key Enabling Technologies project, supported by the Ministry of Education, Youth, and Sports of the Czech Republic. Project No. CZ.02.01.01/00/22_008/0004558, co-funded by the European Union. Views and opinions expressed are, however, those of the authors only and do not necessarily reflect those of the European Union or European Research Executive Agency (REA). Neither the European Union nor the granting authority can be held responsible for them. This work was carried out in the framework of DN-JD-SusMatEner (Doctoral Network Joint Doctorate Sustainable Materials-By- Design for Renewable Energy) and received funding from the European Union’s Horizon MSCA-2023-DN program under the European Research Executive Agency Agreement No. 101168616.

References

1 W. Cao, J. Jiang, X. Xie, A. Pal, J. H. Chu, J. Kang and K. Banerjee, 2-D layered materials for next-generation electronics: Opportunities and challenges, *IEEE Trans. Electron Devices*, 2018, **65**(10), 4109–4121.
2 A. K. Katiyar, A. T. Hoang, D. Xu, J. Hong, B. J. Kim, S. Ji and J.-H. Ahn, 2D materials in flexible electronics: recent advances and future prospectives, *Chem. Rev.*, 2023, **124**(2), 318–419.
3 R. Bian, C. Li, Q. Liu, G. Cao, Q. Fu, P. Meng, J. Zhou, F. Liu and Z. Liu, Recent progress in the synthesis of novel two-dimensional van der Waals materials, *Natl. Sci. Rev.*, 2022, **9**(5), nwab164.

4 C. Song, G. Noh, T. S. Kim, M. Kang, H. Song, A. Ham, M. Jo, S. Cho, H.-J. Chai and S. R. Cho, Growth and interlayer engineering of 2D layered semiconductors for future electronics, *ACS Nano*, 2020, **14**(12), 16266–16300.
5 X. Qin, H. Cui, L. Guo, X. Li and Q. Zhou, Theoretical study of gas sensing toward acetone by a single-atom transition metal (Sc, Ti, V, and Cr)-doped InP3 monolayer, *ACS Omega*, 2024, **9**(45), 45059–45067.
6 P. V. Pham, S. C. Bodepudi, K. Shehzad, Y. Liu, Y. Xu, B. Yu and X. Duan, 2D heterostructures for ubiquitous electronics and optoelectronics: principles, opportunities, and challenges, *Chem. Rev.*, 2022, **122**(6), 6514–6613.
7 Y. Liu, N. O. Weiss, X. Duan, H.-C. Cheng, Y. Huang and X. Duan, van der Waals heterostructures and devices, *Nat. Rev. Mater.*, 2016, **1**(9), 1–17.
8 K. Choudhary, K. F. Garrity, S. T. Hartman, G. Pilania and F. Tavazza, Efficient computational design of two-dimensional van der Waals heterostructures: Band alignment, lattice mismatch, and machine learning, *Phys. Rev. Mater.*, 2023, **7**(1), 014009.
9 X. Niu, Z. Niu, A. Shi, L. Liu, X. Wang and X. Zhang, Interlayer Twist Induces the Formation of Self-Doped p–n Junctions at Atomically Thin Thickness, *Chem. Mater.*, 2025, **37**(15), 5777–5784.
10 A. Rehmat, M. Asim, M. H. Pervez, M. A. Khan, S. Shin, E. Elahi, M. Ahmad, M. Nasim, S. Rehman, S. Kim, M. F. Khan and J. Eom, Floating gate synaptic memory of Janus WSSe Multilayer for neuromorphic computing, *Mater. Today Adv.*, 2025, **27**, 100608.
11 Y. Zhao, Substrate and interface engineering for centimeter-sized wafer-scale growth of crystalline black phosphorus ultrathin films, *PAOYUE-Kong Library*, 2025, 115.
12 B. Huang, Z. Zhao, Y. Zheng, K. Xu, D. Wang, Q. Yang, T. Yang, X. Yang and H. Chen, 2D/3D-printed PEDOT/PSS conductive hydrogel for biomedical sensors, *Int. J. Bioprint.*, 2024, **10**(2), 1725.
13 B. Du, X. Tian, Z. Chen, Y. Ge, C. Chen, H. Gao, Z. Liu, J. Tung, D. Fixler and S. Wei, Ultrasensitive optoelectronic biosensor arrays based on twisted bilayer graphene superlattice, *Natl. Sci. Rev.*, 2025, **12**(10), nwaf357.
14 V. P. Kumar and D. K. Panda, Next generation 2D material molybdenum disulfide (MoS2): properties, applications and challenges, *ECS J. Solid State Sci. Technol.*, 2022, **11**(3), 033012.
15 L. Tao, Z. Chen, Z. Li, J. Wang, X. Xu and J.-B. Xu, Enhancing light-matter interaction in 2D materials by optical micro/nano architectures for high-performance optoelectronic devices, *InfoMat*, 2021, **3**(1), 36–60.
16 Z.-W. Li, Y.-H. Hu, Y. Li and Z.-Y. Fang, Light–matter interaction of 2D materials: Physics and device applications, *Chin. Phys. B*, 2017, **26**(3), 036802.
17 M. Asim, A. Rehmat, M. F. Khan, S.-H. Shin, T. W. Kim and J. Eom, High-Performance Spin Field-Effect Transistors with Multicycle Spin Precession in BLG/WSe2/hBN Heterostructures, *ACS Omega*, 2025, **10**(38), 44365–44373.
18 E. Elahi, S. Nisar, M. Rabeel, M. A. Rehman, M. Ouladsamne, A. Irfan, M. Abubakr, J. Aziz, M. Asim and G. Dastgeer, Gate-controlled rectification and broadband photodetection in a P–N diode based on TMDC heterostructures, *Mater. Adv.*, 2024, **5**(3), 1226–1233.
19 E. Elahi, M. Rabeel, B. Ahmed, J. Aziz, M. Suleman, M. A. Khan, S. Rehman, A. Rehmat, M. Asim and M. A. Rehman, Revealing Bipolar Photoresponse in Multiheterostructured WTe2–GaTe/ReSe2–WTe2 P–N Diode by Hybrid 2D Contact Engineering, *ACS Appl. Mater. Interfaces*, 2024, **16**(40), 54367–54376.
20 M. Suleman, M. Kim, A. Rehmat, E. Elahi, M. Asim, M. Riaz, S. Kumar, J. Jung and Y. Seo, Exploring Double NDR Modulation and UV-NIR Photodetection in MoS2/Sb2Se3 Heterostructures, *Adv. Opt. Mater.*, 2025, **13**(32), e01177.
21 M. Makki, M. Arshad, M. M. Mudassar, M. U. Salman, A. Mahmood, W. Al-Masry, M. Asim and S. Atiq, Linear trends between power output and absorbing layer thickness in next generation high-performance organic perovskite solar cells, *Mater. Today Commun.*, 2025, 113564.
22 T. I. Alam, Synergetic-engineered all van der Waals photodiodes for fast-broadband photodetection and multifunctional optoelectronics, *PAOYUE-Kong Library*, 2025, 134.
23 D. H. Shin and S.-H. Choi, Graphene-Based Semiconductor Heterostructures for Photodetectors, *Micromachines*, 2018, **9**(7), 1–29.
24 Z. Guo, Y. He, H. Wei, D. Jiang, M. Zhao, L. Liang and Y. Wei, Photon-energy-gated carrier accumulation in ordered core–shell nanowires for neuromorphic photodetection and memory, *Laser Photonics Rev.*, 2026, **20**(8), e02268.
25 B. Wang, X. Feng, Y. Liu, X. Wang, E. Liu, Y. Zhao, Z. Miao and Z. Li, Ultrafast electron transfer coupled with a proton relay in an anisotropic dual S-scheme heterojunction for overcoming kinetics mismatch in H2O2 photosynthesis, *Adv. Sci.*, 2026, **13**(14), e22285.
26 B. Gao, Y. Yan, S. Zhang, Z. Wu, Y. Meng, Y. Zhang, W. Wang, Y. Shen, S. Hu, B. Li, H. Shao, P. Xie, S. Yip and J. C. Ho, Precise p-Type Substitutional Doping Enables WS_2 p-n Anti-Ambipolar Homojunction Phototransistor Arrays, *Adv. Funct. Mater.*, 2025, **35**(33), 2425884.
27 W. Ahmad, L. Pan, K. Khan, L. Jia, Q. Zhuang and Z. Wang, Progress and Insight of van der Waals Heterostructures Containing Interlayer Transition for Near Infrared Photodetectors, *Adv. Funct. Mater.*, 2023, **33**(19), 2300686.
28 P. V. Pham, S. C. Bodepudi, K. Shehzad, Y. Liu, Y. Xu, B. Yu and X. Duan, 2D Heterostructures for Ubiquitous Electronics and Optoelectronics: Principles, Opportunities, and Challenges, *Chem. Rev.*, 2022, **122**(6), 6514–6613.
29 S. Li, F. Wang, Y. Wang, J. Yang, X. Wang, X. Zhan, J. He and Z. Wang, van der Waals Ferroelectrics: Theories, Materials, and Device Applications, *Adv. Mater.*, 2024, **36**(22), 2301472.
30 G. Dushaq and M. Rasras, Multilayer 2D germanium phosphide (GeP) infrared phototransistor, *Opt. Express*, 2021, **29**(6), 9419–9428.
31 T. Yu, H. Nie, S. Wang, B. Zhang, S. Zhao, Z. Wang, J. Qiao, B. Han, J. He and X. Tao, Two-Dimensional GeP-Based Broad-Band Optical Switches and Photodetectors, *Adv. Opt. Mater.*, 2020, **8**(2), 1901490.

32 D. Zhang, Y.-C. Wu, M. Yang, X. Liu, C. Ó. Coileáin, M. Abid, M. Abid, J.-J. Wang, I. Shvets, H. Xu, B. S. Chun, H. Liu and H.-C. Wu, Surface enhanced Raman scattering of monolayer MX2 with metallic nano particles, *Sci. Rep.*, 2016, **6**(1), 30320.

33 Z. Zhang and J. T. Yates Jr., Band Bending in Semiconductors: Chemical and Physical Consequences at Surfaces and Interfaces, *Chem. Rev.*, 2012, **112**(10), 5520–5551.

34 M. Bai, Y. Zhao, S. Xu, T. Tang and Y. Guo, Asymmetric bias-induced barrier lowering as an alternative origin of current rectification in geometric diodes, *Commun. Phys.*, 2021, **4**(1), 236.

35 H. C. Card and E. H. Rhoderick, The effect of an interfacial layer on minority carrier injection in forward-biased silicon Schottky diodes, *Solid-State Electron.*, 1973, **16**(3), 365–374.

36 Q. Liu, J.-J. Li, D. Wu, X.-Q. Deng, Z.-H. Zhang, Z.-Q. Fan and K.-Q. Chen, Gate-controlled reversible rectifying behavior investigated in a two-dimensional $${\mathrm{MoS}}_{2}$$ diode, *Phys. Rev. B*, 2021, **104**(4), 045412.

37 L. Xie, S.-Z. Chen, W.-X. Zhou and K.-Q. Chen, Large rectifying ratio in a nitrogen-doped armchair graphene device modulated by the gate voltage, *Org. Electron.*, 2017, **46**, 150–157.

38 H. L. Tan, F. F. Abdi and Y. H. Ng, Heterogeneous photocatalysts: an overview of classic and modern approaches for optical, electronic, and charge dynamics evaluation, *Chem. Soc. Rev.*, 2019, **48**(5), 1255–1271.

39 Y. Guo, W. Shi and Y. Zhu, Internal electric field engineering for steering photogenerated charge separation and enhancing photoactivity, *EcoMat*, 2019, **1**(1), e12007.

40 D. Zhang, W. Zheng, R. Lin, Y. Li and F. Huang, Ultrahigh EQE (15%) Solar-Blind UV Photovoltaic Detector with Organic–Inorganic Heterojunction via Dual Built-In Fields Enhanced Photogenerated Carrier Separation Efficiency Mechanism, *Adv. Funct. Mater.*, 2019, **29**(26), 1900935.

41 J. Cheng, H. Cao, S. Zhang, F. Yue and Z. Zhou, Reinforcing built-in electric field to enable efficient carrier extraction for high-performance perovskite solar cells, *Mater. Chem. Front.*, 2024, **8**(4), 956–985.